Operando phase mapping in multi-material laser powder bed fusion

Shieren Sumarli, Florencia Malamud, Steven van Petegem, Steve Gaudez, Antonios Baganis, Matteo Busi, Efthymios Polatidis, Christian Leinenbach, Roland E Logé, Markus Strobl

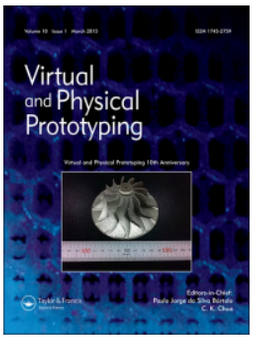

Taylor & Francis
Taylor & Francis Group

Virtual and Physical Prototyping

ISSN: (Print) (Online) Journal homepage: www.tandfonline.com/journals/nvpp20

Operando phase mapping in multi-material laser powder bed fusion

Shieren Sumarli, Florencia Malamud, Steven Van Petegem, Steve Gaudez, Antonios Baganis, Matteo Busi, Efthymios Polatidis, Christian Leinenbach, Roland E. Logé & Markus Strobl

To cite this article: Shieren Sumarli, Florencia Malamud, Steven Van Petegem, Steve Gaudez, Antonios Baganis, Matteo Busi, Efthymios Polatidis, Christian Leinenbach, Roland E. Logé & Markus Strobl (2024) Operando phase mapping in multi-material laser powder bed fusion, Virtual and Physical Prototyping, 19:1, e2429132, DOI: 10.1080/17452759.2024.2429132

To link to this article: https://doi.org/10.1080/17452759.2024.2429132

VIRTUAL AND PHYSICAL PROTOTYPING
2024, VOL. 19, NO. 1, e2429132 (17 pages)
https://doi.org/10.1080/17452759.2024.2429132

Operando phase mapping in multi-material laser powder bed fusion

Shieren Sumarli[a,b], Florencia Malamud[a], Steven Van Petegem[c], Steve Gaudez[c], Antonios Baganis[d,e], Matteo Busi[a], Efthymios Polatidis[f], Christian Leinenbach[d,e], Roland E. Logé[b] and Markus Strobl[a]

[a]PSI Center for Neutron and Muon Sciences, Paul Scherrer Institute, Villigen, Switzerland; [b]Thermomechanical Metallurgy Laboratory – PX Group Chair, École Polytechnique Fédérale de Lausanne (EPFL), Lausanne, Switzerland; [c]PSI Center for Photon Science, Paul Scherrer Institute, Villigen, Switzerland; [d]Laboratory for Advanced Materials Processing, Swiss Federal Laboratories for Materials Science and Technology (Empa), Dübendorf, Switzerland; [e]Laboratory for Photonic Materials and Characterization, École Polytechnique Fédérale de Lausanne (EPFL), Lausanne, Switzerland; [f]Laboratory of Technology and Strength of Materials, University of Patras, Patras, Greece

ABSTRACT

Layer-wise laser-based additive manufacturing techniques offer immense versatility and flexibility in fabricating metallic composites with complex shapes. Interest in producing new multi-materials with advanced characteristics outpaces the available methods that provide insights into the bulk material formation, which in turn enables process and material optimisation. While some advanced operando studies enable highly local observations in the established metallic layers, the effect of intrinsic heat treatment inherent in the process in the bulk of the material is generally beyond reach of operando characterisation. Here, we approach the regime through advanced operando neutron imaging utilising a custom-designed laser powder bed fusion device on a neutron beamline. Operando polarisation contrast neutron imaging experiments were carried out during building centimetre-sized specimens with different powder premixture compositions of 316L and CuCrZr. The results of these full-field spatially resolved measurements reveal the quantitative evolution of ferromagnetic phases and temperature throughout the specimens and processing time.

ARTICLE HISTORY
Received 26 August 2024
Accepted 8 November 2024

KEYWORDS
Operando polarisation contrast neutron imaging; operando neutron temperature mapping; laser powder bed fusion; multi-material processing; ferromagnetic phase quantification

1. Introduction

Laser powder bed fusion (PBF-LB) is a bottom-up, layer-by-layer additive manufacturing (AM) technique most commonly used to produce metallic parts with complex geometries and intricate designs. The process can deliver optimised geometries and, therefore, lightweight parts that conventional manufacturing techniques would hardly produce. Furthermore, the process offers tailorable physical and mechanical properties according to the end use of the parts. The desired properties are achieved by careful control over numerous variables inherent in the process, such as printing parameters, build geometries, and physical and chemical properties of the feedstock materials. The flexibility of designing the feedstock materials, i.e. combining alloys (multi-materials) to fabricate metallic composites with enhanced properties, has received extensive attention in the past decade [1, 2].

Among the multi-materials that can be produced via PBF-LB techniques, combinations of stainless steels (SS) with Cu or Cu alloys have been some of the most widely studied. The aim is to produce parts that simultaneously inherit the excellent mechanical properties and corrosion resistance of SS and the remarkable electrical and thermal conductivity of Cu. Several studies attempted to combine SS and Cu through the PBF-LB process by building one material on top or alongside the other [3–6]. The interfacial microstructure and mechanical properties have been extensively characterised. Liquation cracks were reportedly found at the interface, because in the fusion zone, SS solidifies first while Cu, having lower melting temperature, segregates and forms a fine network of liquid Cu between the SS cells [7, 8]. Upon further cooling, solidification shrinkage combined with residual stress accumulation, which cannot be compensated by the Cu liquid, results in material separation and crack propagation, adversely affecting the mechanical properties.

Other studies used the PBF-LB technique to produce Fe-Cu alloys from their mixed elemental powders [9, 10]. Mixtures of 10, 20, and 50 wt.% Cu in Fe were reported to yield stronger built parts under compression

CONTACT Markus Strobl markus.strobl@psi.ch PSI Center for Neutron and Muon Sciences, Paul Scherrer Institute, Villigen 5232, Switzerland
Supplemental data for this article can be accessed online at https://doi.org/10.1080/17452759.2024.2429132.

than the individual components. However, the presence of liquation cracks compromises their ability to withstand tensile loads. Correspondingly, Wen et al. [11] used a compositional gradient approach to find the optimum 316L and Cu10Sn powder combination for crack-free and high tensile strength builds. Cracks and pores were observed to be present in the parts with Cu10Sn of ≤ 40 wt.% due to restricted liquid feeding in the interdendritic regions. Reliable tensile tests on reasonably dense and crack-free builds revealed superior yield and ultimate tensile strengths of parts with 50–80 wt.% Cu10Sn. Furthermore, their detailed microstructural characterisations coupled with phase field simulations also unveiled the multiple phase transformations occurring during rapid solidification, which led to the formation of γ-Fe, ε-Cu, and α-Fe in the final microstructures.

α-Fe has a body-centered cubic (BCC) crystal structure and is ferromagnetic. The presence of α-Fe in the as-built microstructure of bimetallic 316L and Cu-alloy has been commonly observed [11–13]. Wen et al. [11] suggested that precipitation hardening, facilitated by dislocation looping around the α-Fe particles, contributes to composite strengthening. However, the volume fraction and spatial distribution of this phase have not been investigated. Additionally, owing to the vital role of the α-Fe in enhancing the mechanical properties of the composite, it is highly desirable to gain insight into the conditions assisting the formation and growth of this phase in the bulk during the process. This knowledge would enable the potential to control the α-Fe volume fraction and distribution locally according to the desired physical and mechanical properties in either mixtures or at the interface of the two materials.

Despite the advancements in multi-material additive manufacturing (AM), there remains a significant gap in understanding the microstructural evolution and phase distributions during the fabrication process. Current phase mapping techniques, such as electron backscatter diffraction (EBSD) [14, 15] and optical microscopy with chemical etching [16, 17], have notable limitations. One primary limitation is their destructiveness, which prevents real-time measurements during the manufacturing process and restricts analysis to pre-prepared specimens. Additionally, these methods often provide localised analysis. Non-destructive evaluation techniques, particularly those utilising synchrotron X-ray sources, offer some advantages but are often confined to surface regions or relatively thin geometries [18, 19]. The limitation arises from the high photon absorption in metallic specimens, which can lead to full beam attenuation within a few millimetres or less depending on the X-ray energy used and the material being investigated. In contrast, the superior penetration capabilities of neutrons allow for non-destructive characterisation of bulk metallic materials with thickness up to centimetres [20–22], i.e. the representative bulk volume of PBF-LB-built components.

To facilitate non-destructive data acquisition during the PBF-LB process, a downsized PBF-LB device (n-SLM) was developed within the Applied Materials Group at the Paul Scherrer Institute supporting various neutron characterisation techniques, i.e. neutron diffraction [23, 24], wavelength-resolved diffraction contrast neutron imaging [25–27], polarisation contrast neutron imaging (PNI) [28, 29], and conventional radiography [30]. Amongst these techniques, PNI offers sufficiently high spatial and temporal resolution capable of following phase changes that occur during the PBF-LB process. The technique exploits the high sensitivity of the magnetic moments of neutrons and, thus, is sensitive down to sub-percent fractions of ferromagnetic phases that are present in the stainless steel and Cu alloy composite. In addition to depolarisation, the concurrently probed attenuation, which is sensitive to temperature due to the contribution of the inelastic scattering cross section [31, 32], can also be resolved spatially.

This study emphasises the importance of neutron imaging, in particular PNI, in the context of multi-material AM, specifically for monitoring the evolution of phase distributions and thermal profiles while processing 316L and CuCrZr premixtures using the n-SLM device. This allows correlating temperature conditions with the formation of the ferromagnetic phase. CuCrZr is a precipitation-hardened alloy with good mechanical properties and high thermal conductivity [33–35], and was chosen due to its minor amount (< 1 wt.%) of alloying elements. Premixtures were studied systematically to create investigations in well-controlled chemistries instead of a random concentration of, for instance, an interface. The premixtures used are 40, 50, and 60 wt.% of CuCrZr in 316L due to the fact that the as-built microstructures of such mixtures exhibit a transition between relatively low to high quantities of α-Fe according to Ref. [11] at concentrations below and above 50 wt.%, respectively. A subsequent PNI tomography resolves the 3-dimensional α-Fe distribution in the built specimens. Subsequent postmortem microstructure and magnetisation analyses were carried out to complement the operando analysis. The findings not only enhance the understanding of microstructural evolution but also contribute to optimising the processing parameters for improved and potentially locally tailored material properties in multi-material AM applications.

2. Measurements

2.1. N-SLM setup

The downsized PBF-LB device (n-SLM) has the basic functionalities of PBF-LB machines available on the market and was adjusted and optimised for installation and alignment in neutron imaging and engineering diffraction instruments, in particular those at the Swiss Spallation Neutron Source (SINQ). The main configurations of the device are shown in Figure 1, and the numbered components are described in detail in the Methods section. The n-SLM functions like a conventional PBF-LB additive manufacturing machine; First, the build plate is lowered by a desired layer thickness, and subsequently, the powder deposition system moves back and forth to spread a new thin layer of powder on top. Finally, a focused high-power laser beam selectively melts and fuses the powder according to a predefined geometry. This series of steps is repeated multiple times until the desired 3D structure is attained. The experiment was conducted at the BOA beamline [36] of the PSI. Figure 2 shows pictures of the experimental setup detailing some of the components utilised. Neutron images are acquired continuously throughout the PBF-LB process. The start of a print and the acquisition are synchronised but subsequently run independently.

2.2. Operando neutron imaging

The scanning unit was adjusted such that the resulting spot diameter at $1/e^2$ was 55 µm, and the laser source was set in continuous-wave operation mode. Supplementary Figure 2 shows the parallelepiped specimens that were built for each composition on the Ø20 mm 316L build plate setting layer thicknesses of 30 µm, a hatch distance of 85 µm, and a target dimension of $10 \times 10 \times 15$ mm^3 (x-TD2, z-TD1, y-BD). The laser was operated at 165–195 W, depending on the weight percent of the CuCrZr powder, with a scanning speed of 425 mm/s and a scanning strategy of bidirectional 90° interlayer rotation. The laser power increases by 15 W with each 10 wt.% CuCrZr increase in the CuCrZr content. The different input energies were used as CuCrZr has lower absorptivity compared to 316L [37] and have been evaluated in advance through offline test printing. The surrounding temperature and atmospheric conditions were not actively controlled and can be assumed to have largely remained at ambient levels throughout the experiment. However, an inert atmosphere was maintained with a continuous flow of high-purity Ar to prevent oxidation and ensure uniform environmental conditions across all specimens.

The neutron images, including the open beam, were alternately recorded for spin-up and spin-down configurations and corrected by dark-current background measurements. During the operando experiment, images were acquired with an exposure time of 10 s and data recording of 5 s for each spin state. This exposure time allows to follow the layer-wise printing of two steps, which takes around 15 s per layer. After printing was finished, the powder surrounding the specimen was removed, and a tomographic scan over 360° with a rotation step of 1° was performed with the entire machine still in place, using the specially designed rotation stage of the n-SLM. The exposure time used was 50–80 s per spin, i.e. 100–160 s per projection. It is noted that the time variations are due to neutron source instabilities.

The distribution of low ferromagnetic phase fractions in the bulk of a material can be analysed by spatially resolved detection of the depolarisation of an initially polarised collimated incident neutron beam after transmitting through the material [38, 39]. Despite having exceptional sensitivity down to 2×10^{-2} vol.%, the technique is, however, unable to distinguish different phases exhibiting ferromagnetism with the same crystal structure. The depolarisation coefficient η for a ferromagnetic material with randomly oriented domains is deduced in Ref. [39] by

$$\eta = \frac{\gamma^2 B^2 d}{3v^2}\, c \tag{1}$$

where γ is the gyromagnetic factor of the neutron, B is the magnetic field of the domains which interact with the neutron spin, d is the domain size, v is the neutron velocity, and c is the concentration factor of the ferromagnetic phases in the probed specimen. In this study, d is considered constant with temperature across the field of view (FoV). Domain wall motion and, thus, the growth of d highly depends on the microstructure and is typically hindered by domain wall pinning sites, e.g. dislocations and grain boundaries [40, 41]. High dislocation densities in 316L [42] and pure Cu [43] manufactured by the PBF-LB technique are typical. Wang et al. [43] and Bertsch et al. [44] concluded that the origin of the observed high density dislocations is specific to the processing route where repeated compression and tension cycles are inherent in AM. Zafari and Xia [9, 10] observed ultrafine equiaxed grain structure, hence, high density of grain boundaries in the PBF-LB-built Fe-Cu systems.

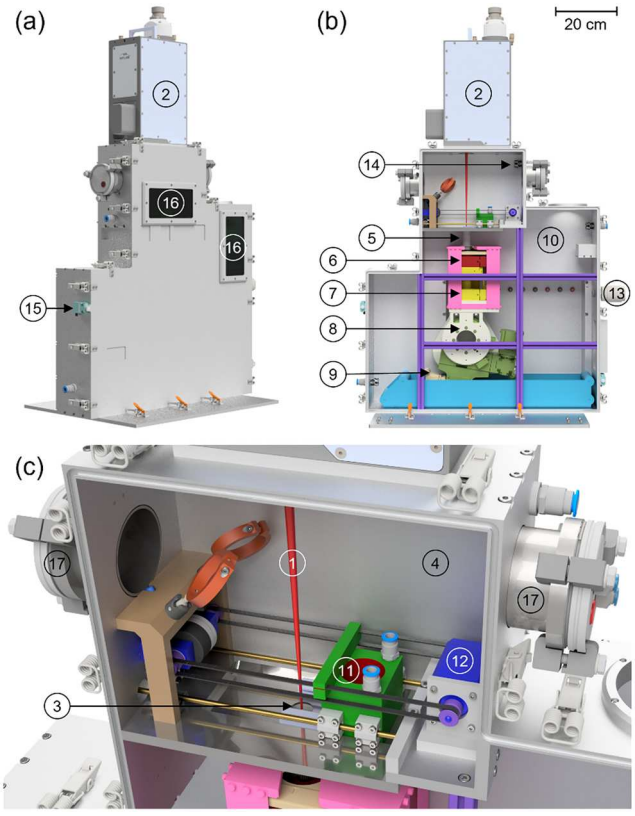

Figure 1. 3D model of the n-SLM device: (a) with the door installed, (b) open chambers displaying its interior, and (c) zoomed-in open printing chamber. The numbered components represent 1) laser beam, 2) 3-axis scanning unit, 3) build plate opening, 4) printing chamber, 5) Al cylinder holder, 6) rotation stage, 7) vertical translation stage, 8) goniometer stage, 9) linear translation stage, 10) drive chamber, 11) powder reservoir, 12) stepper motor, 13) safety relief valve, 14) filter cap, 15) position switch, and 16) observation windows, and 17) vacuum flanges.

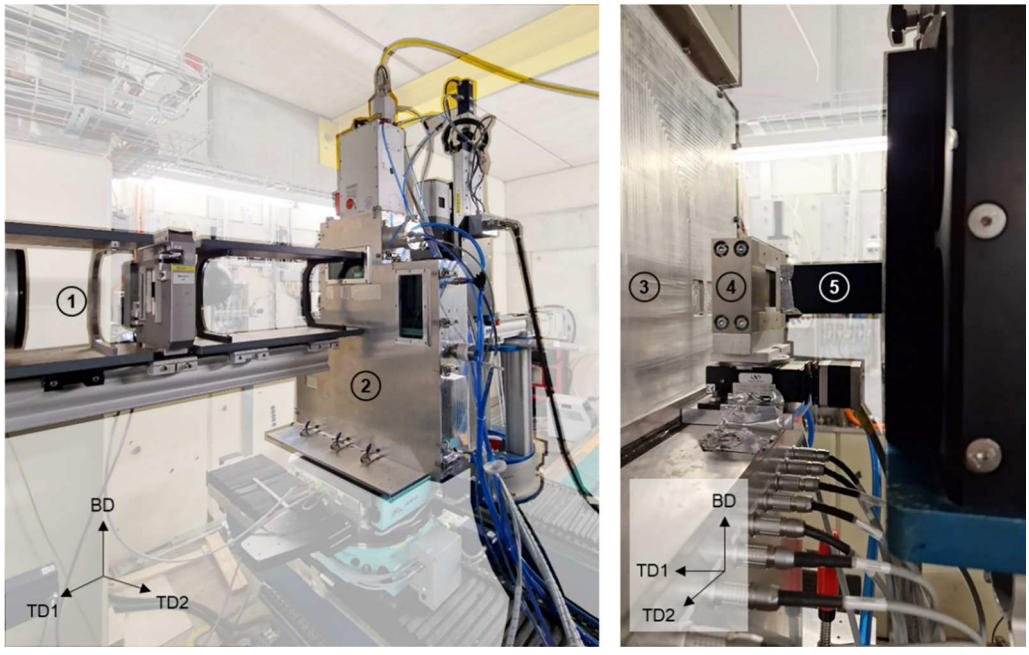

Figure 2. The n-SLM installed within the PNI setup at the BOA beamline: 1) magnetic guide field, 2) front door of the n-SLM, 3) back part of the n-SLM, 4) spin analyzer, and 5) small scale extension of the detector box.

As the concentration factor c can, thus, be assumed the only variable in the line integral of the depolarisation coefficient along the neutron path, which constitutes the measurement according to the Beer–Lambert law, it can be deduced directly from the measurement in each pixel of the image of the specimen. However, during printing, the bulk of the specimens is at elevated temperatures, and the magnetic field B of the magnetic domains of the ferromagnetic phase depends on temperature. The temperature distribution $T(x, y, t)$ throughout the specimens depends on their specific local heat transfer characteristics and the laser energy input. It is, therefore, necessary to deconvolute the effect of temperature on B and, thus, on the depolarisation coefficient, before converting η into the volume fraction of the ferromagnetic phase. The magnetic field B is directly proportional to the magnetisation M and, hence, the magnetic moment m of the specimen, which is expressed by

$$B(T) = \mu_0 M(T) = \mu_0 \frac{m(T)}{V} \tag{2}$$

where V is the specimen volume, which is assumed constant with T, and μ_0 is the permeability of free space, with a specific value of $4\pi \times 10^{-7}$ N/A^2. The magnetic moment m of the specimen with 60 wt.% of CuCrZr was measured as a reference over a temperature range of 300–600 K. The result is plotted in Figure 10(b), which could be used together with the temperature maps to correct for the temperature effects on the depolarisation signal and, thus, the analyses of the concentration of the ferromagnetic phase.

3. Results and discussion

3.1. Operando phase mapping

For the analyses of the phase and temperature evolution, a binning of 200×5 pixels, covering the full lateral (TD2) dimension of the specimen and 250 µm vertically (BD), was performed. The vertical binning corresponds to the achievable spatial resolution. Thus, this approach allows for optimisation of the measurement accuracy, particularly in regions with low ferromagnetic phase fractions, without compromising the spatial resolution. The vertical dimension of the binning is equivalent to approximately 8 printed layers. The view on the topmost 2 mm of the specimen was obstructed by the steel plate supporting the recoater, i.e. the floor plate of the printing chamber and, therefore, is omitted

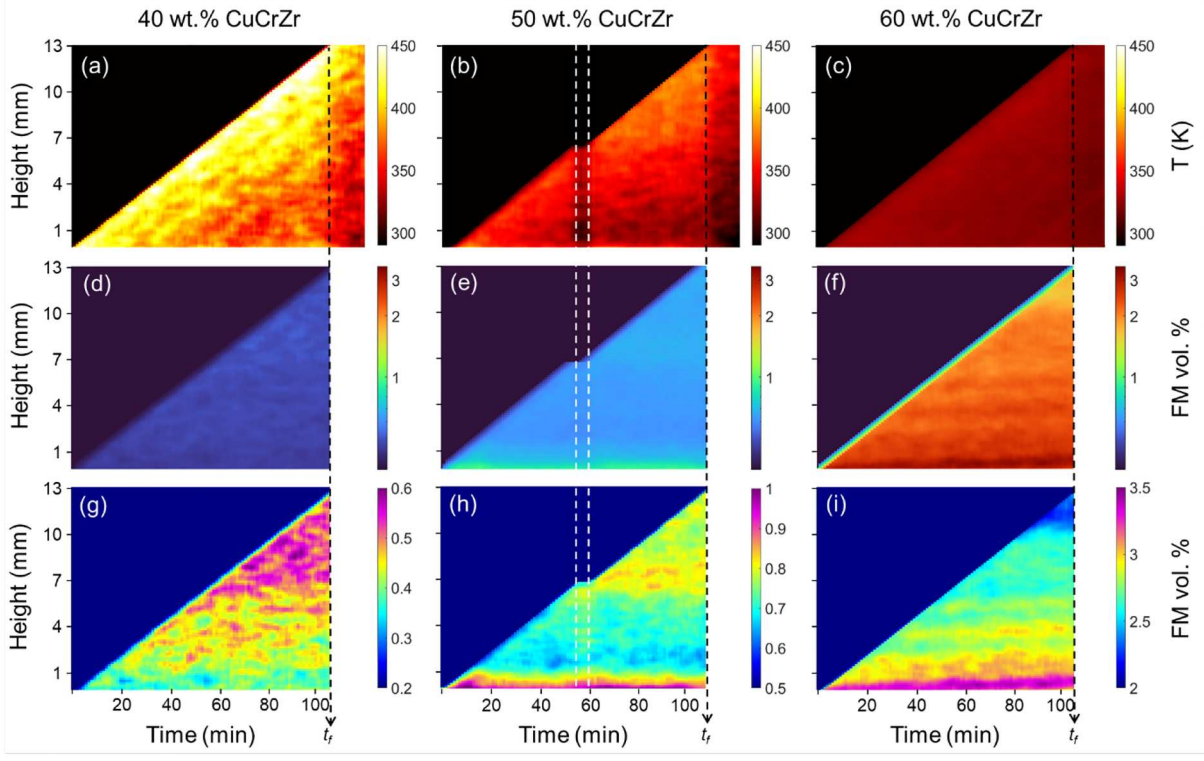

Figure 3. Maps of the temperature evolution (a – c), phase evolution on the same scale for all three specimens (d – f), and phase evolution on individual scales for each specimen (g – i) of the bulk with 40 wt.% CuCrZr (a,d,g), 50 wt.% CuCrZr (b,e,h), and 60 wt.% CuCrZr (c,f,i).

from the analysis. Figure 3 displays the main results of the operando PNI experiments, where the horizontal binning allows to represent the entire process in a single map relative to each parameter considered. The x-axes correspond to the process time, while the progression of the build height is relative to the y-axes of the plots. The colours of the maps correspond to the evolution of temperature in Figure 3(a – c) and of the ferromagnetic phase fraction (FM vol.%) on the same logarithmic scale for all specimens (Figure 3(d – f)), highlighting the very different forming phase fractions relative to the CuCrZr content, and scaled individually for three specimens from minimum to maximum values (Figure 3(g – i)) in order to visualise the phase evolution within each specimen.

The temperature maps are based on the temperature dependence of the beam attenuation due to increasing inelastic scattering cross section with temperature [31]. A linear approximation of the increase of $\mu_s(y, t)$ with temperature based on theoretical considerations and calculations utilising the NCrystal software [45], and validated at RT was applied to calculate the individual $T(y, t)$ temperature maps in Figure 3(a – c). Figure 3(a – c) shows a distinct decrease in overall bulk temperatures for $t > t_f$, which represents the cool-down phase to RT after the end of the printing process. Slightly increasing the input energy with increasing CuCrZr content in the feedstock powders improved the specimen density, which ranges from 96.9–98.3%, with the minimum and maximum values referring to the specimens with 40 and 60 wt.% CuCrZr, respectively. Although the energy density was increased, a temperature decrease from a maximum of 466 K to 406 K to 353 K with increasing CuCrZr content is evident. Cu has nearly 4–5 times higher thermal conductivity than Fe, Ni, and Cr and, therefore, specimens with more Cu content conduct and dissipate heat faster.

During PBF-LB, the previously built layers down to the whole volume inevitably experience cyclic heating and cooling, i.e. an intrinsic heat treatment (IHT). The IHT is well-known to be able to influence the microstructure and mechanical properties of as-built parts [46, 47]. The IHT is characterised by fluctuating temperatures that decrease exponentially within a given volume, which is evidently maintained by the specimens in this study. An incidental interruption during the printing of the specimen with 50 wt.% CuCrZr was observed to slightly decrease the bulk temperatures by about 20–30 K depending on the height. The interruption occurred for roughly 4 minutes and is marked by white dashed lines in Figure 3(b), (e), and (h). The temperature then increases again as the print continues.

The retrieved temperature evolution maps $T(y, t)$ were then used to deconvolute the effect of temperature on the magnetisation of the ferromagnetic domains of the ferromagnetic phase and, thus, the measured depolarisation in order to obtain the correct values of the ferromagnetic phase fractions at $t < t_f$. To this end, the depolarisation coefficient had to be calibrated by reference measurements at RT in order to obtain the evolution of the volume fraction of the ferromagnetic phases during the printing of each specimen on a quantitative scale [28]. The FM volume fraction increases with increasing CuCrZr content, with the largest increase (~4x) between 50 and 60 wt.%.

The phase evolution maps in Figure 3(g – i) show that the evolution of the microstructure is different for the specimen with 40 wt.% CuCrZr as compared to the other two specimens. The FM volume fraction in the 40 wt.% CuCrZr specimen is relatively low close to the build plate and rises significantly with increasing distance from the build plate as more layers were printed up to approximately half of the height, while in the other two specimens, the highest FM volume fraction is found close to the build plate. The incidental print interruption of the 50 wt.% CuCrZr specimen inflicted another rise in FM volume fraction over a thickness of about 3 mm that was built after the interruption. Subsequently, the FM volume fraction drops again as more layers were printed. For the specimen with 60 wt.% CuCrZr, no interruption of printing occurred, and the FM volume fraction gradually decreased with height overall.

3.2. Post-mortem PNI tomographic scans

Figure 4 shows the reconstructed and segmented tomograms of all three specimens, revealing the 3-dimensional interior structure of the ferromagnetic phase distribution in the as-built specimens with different colour scales. The ferromagnetic phase distribution across the BD of each specimen matches the results of the operando experiments very well. Figure 4(a) indicates not only that the specimen with 40 wt.% CuCrZr exhibits a lower FM volume fraction closer to the build plate, but also that the FM volume fraction decreases along TD1. A variation along this direction is not resolved in the operando experiment as the measured values are averaged along the beam direction, which in this case coincides with TD1. While the FM volume fraction in the 40 wt.% CuCrZr specimen throughout the BD and TD1 directions is unevenly distributed, no significant trend was observed along TD2.

In contrast, the specimen with 50 wt.% CuCrZr contains around 1.5 times more FM phase in the vicinity of

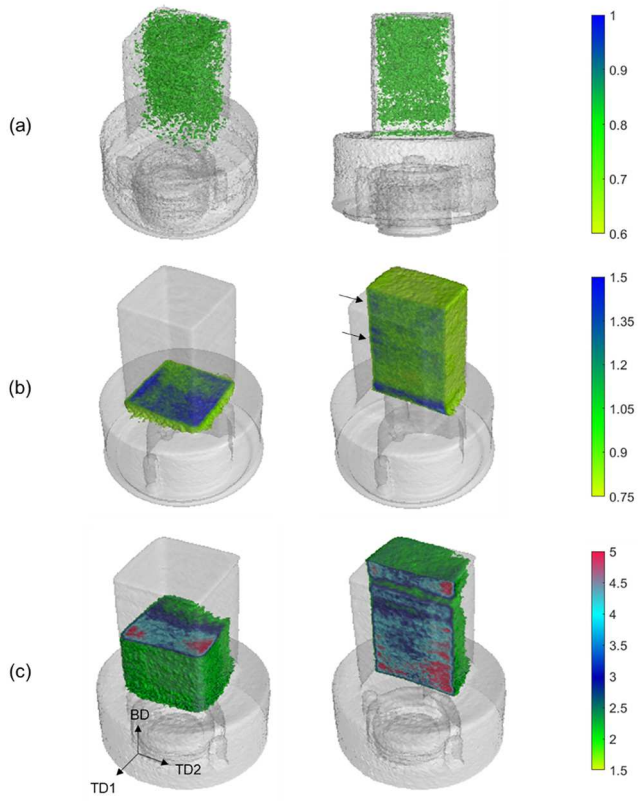

Figure 4. Reconstructed and segmented tomograms of the as-built specimens with (a) 40, (b) 50, and (c) 60 wt.% CuCrZr. The colour bars represent the FM vol.% of the specimens.

the build plate within about 1 mm in height, as compared to the rest of the specimen. Around the mid-height of the specimen, where the interruption occurred during printing, an increase followed by a slight fluctuation of FM volume fraction is apparent. These effects were also observed operando. The FM volume fraction continues to decrease until approximately 2 mm below the top surface, which is not observable during operando experiments, where it rises slightly again. These discerned increments marked by the arrows in Figure 4 (b) are inhomogeneous across TD2, which is more prominent in the region with higher FM volume fraction. Looking at the distribution in TD1 and TD2 close to the build plate, an increased FM volume fraction is found towards the highest TD1 values.

Similar to the specimen with 50 wt.% CuCrZr, the 60 wt.% CuCrZr specimen also exhibits inhomogeneity in ferromagnetic phase distribution in all orthogonal directions. However, as the FM volume fraction of the specimen is generally much higher, the heterogeneity is much more pronounced. Throughout the height of the specimen, the FM volume fraction progressively drops from the build plate up to ~2 mm below the top surface, before it rises again. A substantial gradient across the TD1 with increasing values of TD1 is perceived, exhibiting an FM volume fraction close to 5% towards the corners at the largest and lowest TD2 values. At some heights, elevated FM volume fractions are also observed towards the highest TD2 values. These mainly follow the described trend along the building direction.

3.3. Post-mortem microstructural analysis

In order to correlate the findings from the operando and tomography experiments to the corresponding microstructures, cross sections of the specimens were analysed. The microstructure of each specimen exhibiting the BCC phase within the FoV was selected and is shown in Figure 5. Figure 5(a–c) displays the inverse pole figures along the y direction (IPFY), i.e. the BD, of cross sections with 40, 50, and 60 wt.% CuCrZr, respectively. Figure 5(d–f) shows the corresponding phase maps. The microstructure of the cross section with 40 wt.% CuCrZr mainly consists of columnar elongated grains with a small fraction of equiaxed grains. The analysis of the IPFY map indicates nearly random crystallographic texture, while the phase map shows the presence of the BCC phase (green) randomly distributed among the FCC phase (red). A nearly spherical grain is observed to be fully BCC phase. More fine equiaxed grains are found in the cross section with 50 wt.%

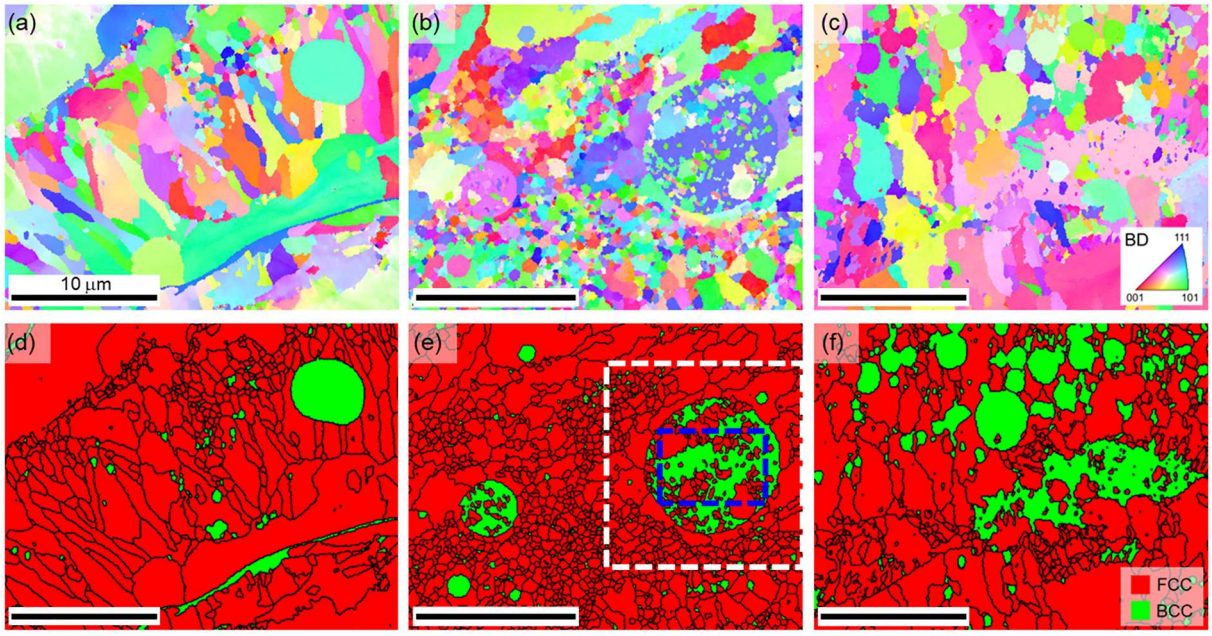

Figure 5. Representative IPFY maps (a – c) and phase maps (d – f) of the cross sections with 40 wt.% CuCrZr (a,d), 50 wt.% CuCrZr (b, e), and 60 wt.% CuCrZr (c,f).

CuCrZr, a few of which are the BCC phase. Some spherical grains varying in size are either fully BCC or partially BCC within which smaller FCC grains are embedded. The analysis of the IPFY map of the cross section also indicates nearly random crystallographic texture, within the analysed area. More spherical and equiaxed grains with BCC phase are observed in the cross section with 60 wt.% CuCrZr. On top of that, fine FCC grains also appear enclosed in an elongated BCC grain with a length of roughly 15 µm.

According to the pseudo-binary equilibrium phase diagram calculated in [11], in which the same main constituents Cu, Fe, Cr, and Ni of 316L and CuCrZr were taken into consideration, the as-built microstructure comprises of ε-Cu, γ-Fe, and α-Fe at room temperature. Among these phases, α-Fe is the only one with BCC crystal structure and exhibits ferromagnetic properties. The microstructure formation mechanism upon solidification could be understood through 2-dimensional phase-field simulations [11]. The sequence of phase transformation was described to be, first, separation of an assumed homogeneous liquid into Fe-rich liquid L(Fe) and Cu-rich liquid L(Cu) at 1653 K. The composition of L(Cu) is inhomogeneous throughout, with higher Cu content at its core and richer in Fe at the surface layer. As the L(Cu) stops growing, L(Fe) starts to solidify as γ-Fe at locally higher Fe concentration regions, followed by solidification of L(Cu) as ε-Cu. Finally, at temperatures below 870 K, γ-Fe transforms partially into α-Fe. However, this sequence does not fully explain the presence of FCC grains with different crystallographic orientations enclosed within the BCC α-Fe grain, as observed in the cross sections for specimens with 50 and 60 wt.% CuCrZr (Figure 5(e,f)).

To better understand this phenomenon, the solid-state phase transformations that occur at relatively low temperatures are considered, which are known to exhibit specific crystallographic orientation relationships (OR), particularly the Kurdjumov – Sachs (K-S) orientation relationship [48]. The K-S OR of the representative FCC and BCC grains indicating partial transformation in the cross section marked by the blue dashed rectangle in Figure 5(e) was analysed using the open-source crystallographic toolbox MTEX (version 5.10.2) [49]. If the surrounding BCC grain partially transforms from γ-Fe and the finer FCC grains are the retained γ-Fe, it implies that various parent orientations transform into one specific child orientation, which is highly improbable. Therefore, the K-S OR analysis was performed by considering the BCC grain as the parent grain, the FCC grains as the child orientation variants, and the inverse of the orientation relationship. Figure 6(a) shows the pole figures reflecting the partial coincidence of the BCC (green) and FCC (red) poles, which are overlayed by the ideal K-S OR (black). The mean angular deviation between the ideal K-S OR and all parent-to-child misorientations is 4.86°. Naraghi [50] reported K-S-defined phase boundaries with deviations of up to 5° in AISI204Cu steel at 60% nominal strain and AISI301 after austenitization and quenching in liquid nitrogen.

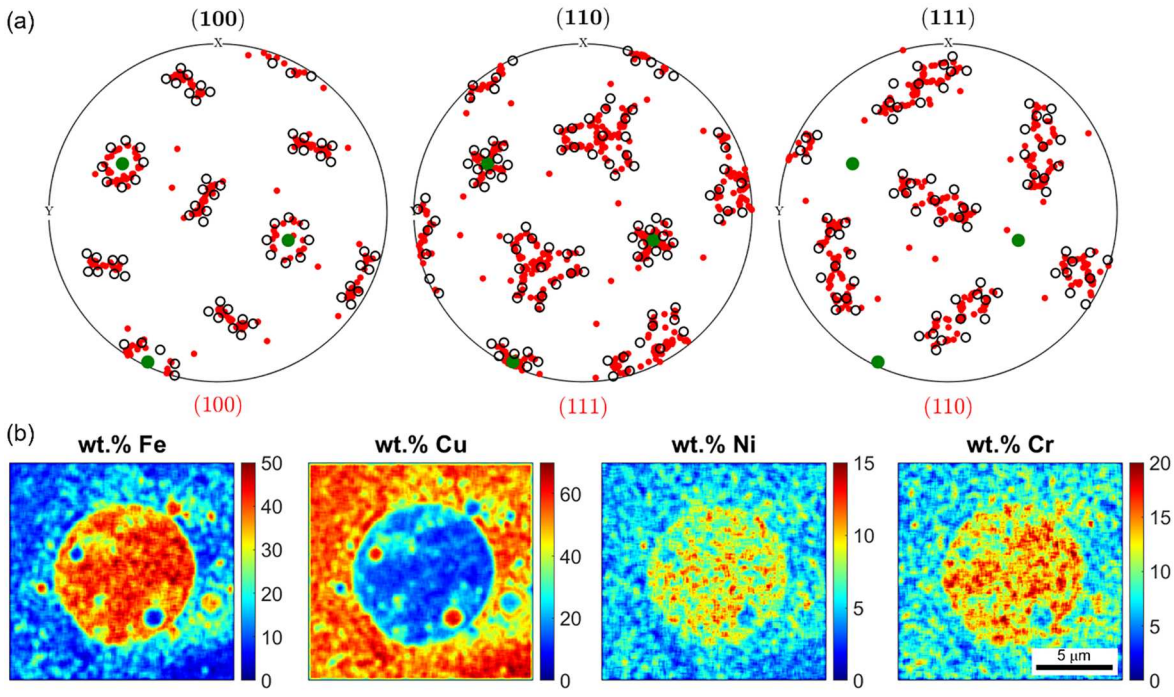

Figure 6. (a) Pole figures showing the ideal K-S orientation relationship (black) overlayed on the actual crystallographic orientation relationship, and (b) processed EDX elemental maps of the marked areas, i.e. white dashed rectangles in Figure 5(e).

To get insight into phase composition, energy dispersive X-ray spectrometer (EDX) analysis was carried out on and surrounding the marked area, i.e. the white dashed rectangle in Figure 5(e). The elemental maps of the main constituents Fe, Cu, Ni, and Cr are shown in Figure 6(b). The maps indicate that the BCC grains are richer in Fe, Ni, and Cr than the surrounding region rich in Cu, i.e. ε-Cu. Two fine spherical ε-Cu domains are embedded in the large spherical Fe-rich region, which implies the presence of both ε-Cu and γ-Fe within the α-Fe grain. The ε-Cu FCC grains are formed upon solidification and, thus, do not have orientation relationships with the enclosing α-Fe BCC grain, which explains the random FCC poles in Figure 6(a). On the other hand, the EDX analysis indicates that the FCC grains have partial coincidence with the BCC grain, suggesting a crystallographic orientation relationship between the two phases, with FCC zones generally containing higher Cu content than the surrounding BCC matrix. It implies that an austenite reversion (α-Fe → γ-Fe) can occur during printing, as Cu stabilises γ-Fe in steels [51]. This may explain the horizontal fluctuation in FM volume fraction observed in Figure 3. The reversion during manufacturing can take place due to the IHT inherent to the process. This was also observed by Mooraj et al. [52] in maraging 250 steel during wire-arc directed energy deposition and by Krakhmalev et al. [53] in martensitic stainless steel during in situ heat treatment.

Electron backscatter diffraction (EBSD) analysis was performed on the cross section with 50 wt.% CuCrZr in areas with distinctly different FM vol.%, i.e. at 0.5, 4, 7, and 12 mm above the build plate and the results are displayed in Figure 7. The grain size range spans from submicron to a few tens of microns. The nonindexed regions on the IPFY maps correspond to grains with equivalent diameters smaller than the step size (0.2 μm). At the height of 0.5 mm, 20.1% of the total mapped cross section consists of very fine grains (< 0.3 μm). Further away from the build plate, the fraction of these fine grains decreases rapidly. Cross sections at 0.5 and 7 mm above the build plate retain considerably more grains with sizes between 1 and 20 μm compared to the other two analysed cross sections. The maximum equivalent grain diameters of the cross sections at 0.5, 4, 7, and 12 mm are 22.2, 38.3, 33.2, and 46.2 μm, respectively.

The distinct difference in grain size distribution suggests different thermal histories in these regions. In the region very close to the build plate (0.5 mm), the layers were printed on relatively cooler substrates and, thus, heat was dissipated faster and the cooling rate was higher. Further away from the built plate (4 mm), the preceding layers experienced intense reheating (IHT), while the subsequent layers were printed on reheated substrates. Therefore, the IHT induced a lower cooling rate and promoted grain growth. Since the printing was incidentally interrupted at around the

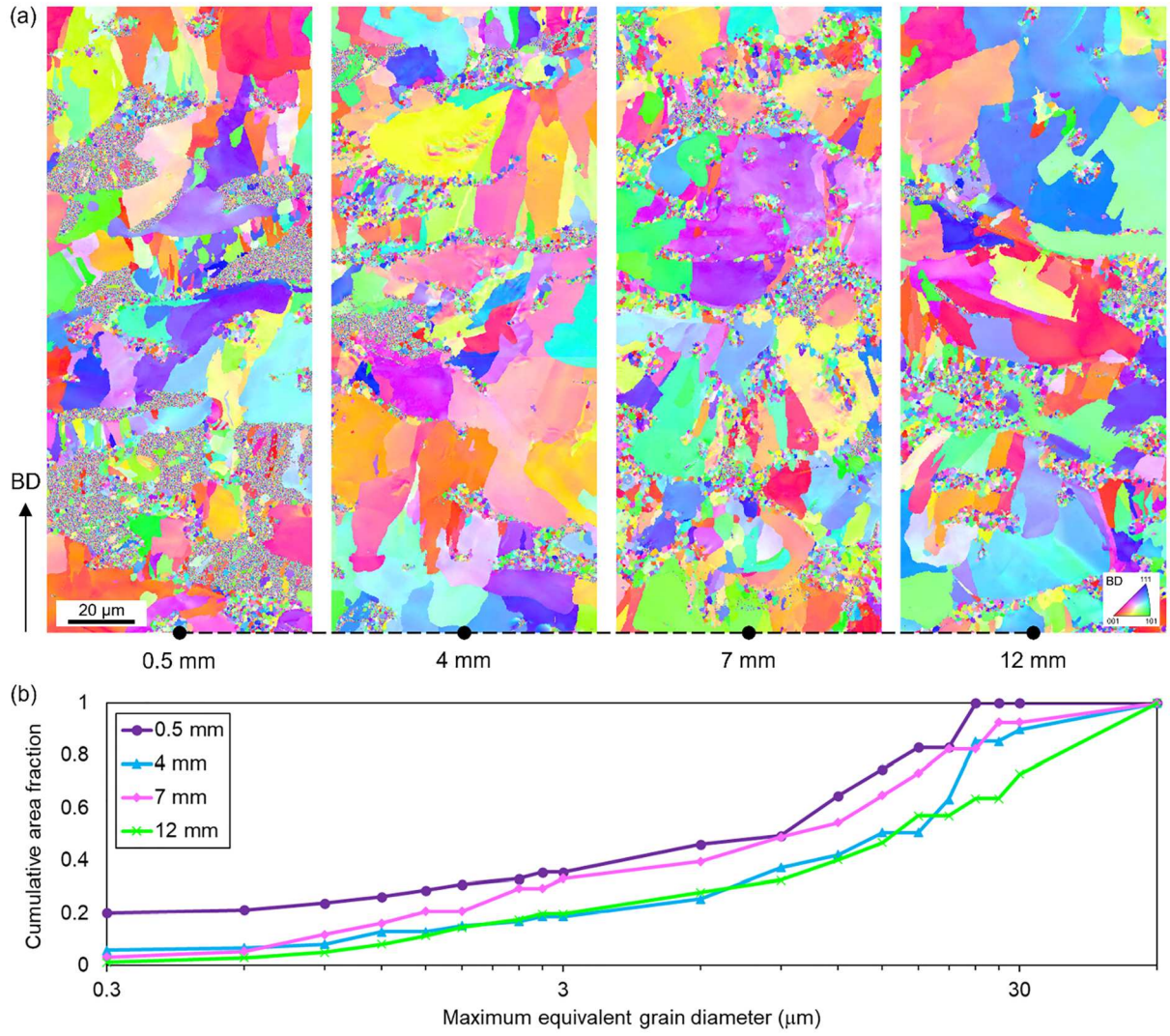

Figure 7. (a) IPFY maps of the cross section with 50 wt.% CuCrZr taken in regions at 0.5, 4, 7, and 12 mm above the build plate and (b) grain size distribution analysis of the corresponding maps.

height of 7 mm, the reheating of the last layers before interruption was less pronounced, which slightly increased the cooling rate and inhibited grain growth. As the printing continued, the grains kept growing.

At temperatures where separation of the single liquid takes place, Fe-rich L(Fe) and Cu-rich L(Cu) liquids are formed rapidly. Chemical separation continues, for example, Ni atoms, which are present in both liquids, prefer to diffuse into the L(Fe) since Ni has a stronger attractive interaction with Fe than Cu, i.e. exothermic enthalpy of mixing [54]. Cooling rates play a decisive role in the final amount of Ni in each liquid just before they solidify. High cooling rates limit the time for Ni to diffuse to L(Fe), and vice versa. As L(Fe) solidifies first, the higher the cooling rates, the higher the amount of Ni that remains in L(Cu). Therefore, the solidified Fe is depleted of Ni, which is a strong austenite stabiliser, causing it to be partially primary α-Fe and partially primary γ-Fe. Solidification of L(Fe) with varying local chemical compositions might follow different solidification paths of steels [55, 56]. Concurrently, interdiffusion also occurs between Fe and Cu atoms; Fe atoms in L(Cu) are expelled to L(Fe) while Cu atoms in L(Fe) are expelled to L(Cu), as the solubility limit of Fe and Cu in L(Cu) and L(Fe), respectively, decreases significantly with temperature [57, 58]. At lower temperatures, in the solid state, depending on the extent of interdiffusion of the elements and IHT, i.e. the local chemical composition, primary γ-Fe and α-Fe might partially transform into secondary α-Fe and γ-Fe, respectively.

The difference in cooling rates and the extent of IHT could explain the variation in FM volume fraction throughout the height of the specimen with 50 and 60 wt.% CuCrZr. In the regions close to the build plate

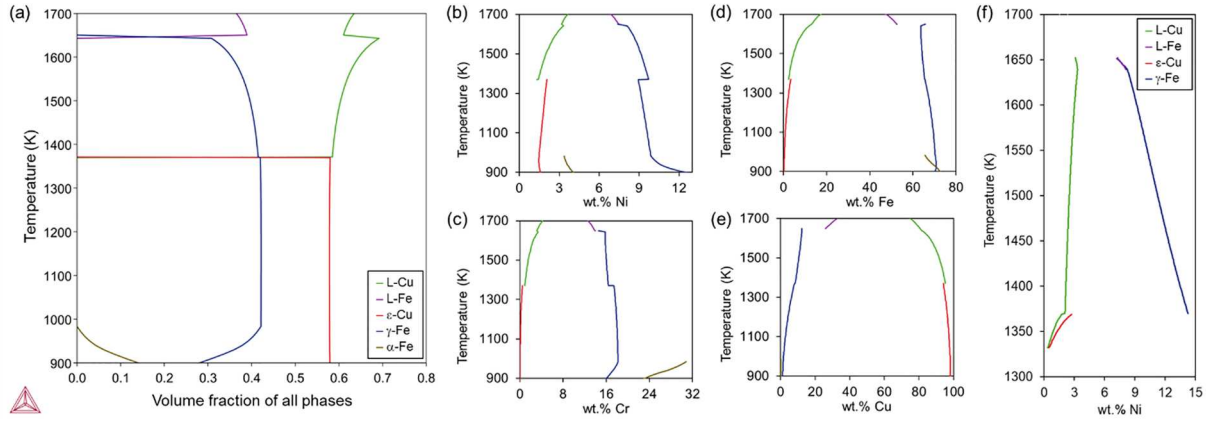

Figure 8. Metastable One-Axis calculation result: (a) volume fraction of all phases; (b) Ni, (c) Cr, (d) Fe, and (e) Cu content in the phases upon solidification, and Scheil-Gulliver calculation result showing (f) Ni content in the phases with decreasing temperature. The results demonstrate the phase stability and transformation predictions for the CuCrZr and 316L alloy system. The x-axis represents the composition, i.e. the volume fraction of the phases (a) and weight fraction of the elements in the system (b–f), while the y-axis shows the temperature (K). The different coloured lines indicate the phase boundaries between various phases, i.e. Fe – or Cu-rich liquid, γ-Fe, α-Fe, and ε-Cu, as calculated by the Thermo-Calc software.

and after printing interruption in the specimen with 50 wt.% CuCrZr, where printing was performed on a substrate with relatively low temperatures, cooling rates play a more dominant role in the interdiffusion phenomena and, thus, in the increased formation of α-Fe of the final microstructure, as supported by the finer grain size distribution in Figure 7. Upon further printing, while increased IHT gradually decreases cooling rates, IHT also promotes diffusion in the solid state, which induces austenite reversion and further decreases the FM volume fraction with increasing height. The somewhat increased FM volume fractions of both specimens in the last printed layers can be explained by the more dominant influence of IHT in this region. The top layers of the specimens underwent less IHT while the cooling rates did not change much and, hence, less austenite reversion occurred, and the final FM volume fraction increased again.

The explanation further justifies the FM volume fraction gradient tendencies along TD1 in both specimens. Along this direction, parallel to the incident neutron beam direction, fresh laminar Ar gas was continuously blown from one side and suctioned on the other. The unidirectional gas flow potentially played a role in altering the cooling rate between the two sides. The region with higher FM phase fractions was in contact with cooler gas, which experienced increasing temperatures towards the exhaust due to interactions with hot specimen and printing by-products and, thus, cooled the formed layers less on that side. The cooling is efficient in the corners of the front side, where the highest FM volume fractions are also found. On top of that, it is shown that the higher the CuCrZr content in the premixture, the faster heat is dissipated from the bulk, i.e. the higher the cooling rate and the lower the IHT, and, therefore, the higher the BCC content formed, which is in agreement with [13].

To confirm the hypothesis of elemental interdiffusion in the investigated alloy systems, metastable One-Axis and Scheil-Gulliver calculations were performed with Thermo-Calc 2023b [59] using the TCFE7: Steel and Fe-alloys database by considering the chemical composition of the main constituents of the specimens with 60 wt.% CuCrZr, i.e. Fe, Cr, Ni, and Cu. The result of the metastable One-Axis calculation is shown in Figure 8(a – e). The plots indicate that above the solidus temperature of L(Fe), the Ni content in L(Fe) increases slightly. The increase in Ni content is also observed in γ-Fe with decreasing temperature. In contrast, a decreasing Ni content in L(Cu) above its solidus temperature and in the solidified ε-Cu is apparent. This opposing trend of Ni content in the two liquids and solid phases is an indication that Ni diffuses out of L(Cu) towards L(Fe), as well as from ε-Cu to γ-Fe. On the other hand, the Cr content, as one of the α-Fe-stabilising elements, only follows the trend of Ni in the liquids while very little change in the solids is seen. As temperature decreases, the amount of Fe and Cu in L(Cu) and L(Fe), respectively, decreases substantially. The metastable One-Axis calculation demonstrates a good agreement with the Scheil-Gulliver calculation shown in Figure 8(f). The Scheil-Gulliver calculation is depicted from the onset of the solidification of γ-Fe, where both L(Cu) and L (Fe) are present. When γ-Fe completely solidifies at 1639 K, enrichment of Ni in γ-Fe prevails as L(Cu)

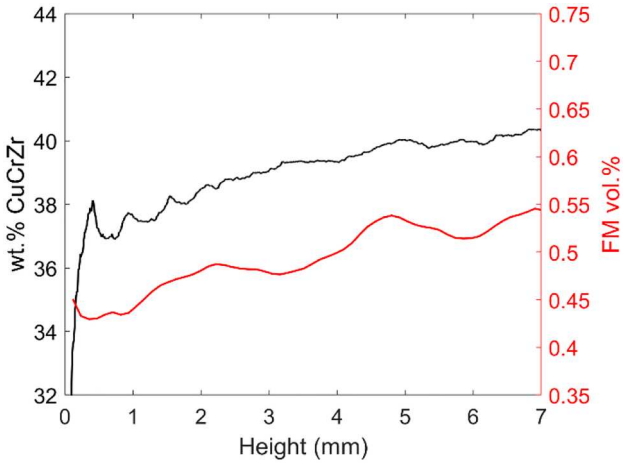

Figure 9. Mean value of the estimated CuCrZr content from EDX analysis and FM volume fraction deduced from the operando PNI experiment over the height from 0 to 7 mm of the specimen with 40 wt.% CuCrZr.

continues to be depleted of Ni until Cu solidification ends, which marks the end of the simulation.

However, these trends of FM volume fraction along TD1 and BD are not found in the specimen with 40 wt.% CuCrZr. A plausible reason could be that the lower Cu content causes the specimen to retain the heat longer, i.e. lower overall cooling rates compared to the other two specimens. Another potential explanation is that below 40 wt.% liquid separation and, thus, Ni entrapment in the Cu-rich liquid is much less prominent. Therefore, slight local fluctuations in chemical composition will either hinder or promote the corresponding α-Fe formation. Based on EDX analysis along the BD of the specimen with 40 wt.% of CuCrZr shown in Figure 9, in regions very close to the 316L build plate, the Cu content, i.e. the estimated fraction of CuCrZr, is relatively lower than in the rest of the bulk, which eventually suppresses the phase transformation.

4. Conclusion

A custom-designed PBF-LB device successfully enabled operando studies of the microstructure evolution during PBF-LB of 316L and CuCrZr powder premixtures. It is demonstrated that polarisation contrast neutron imaging is suitable for time-resolved imaging of bulk properties during the manufacturing of centimetre-sized specimens, providing spatially-resolved maps of the ferromagnetic phase and temperature evolution. Key findings include:

1. Variations in CuCrZr content influenced the bulk temperature profile and ferromagnetic phase volume fraction, where higher contents increased cooling rates and reduced intrinsic heat treatment (IHT), subsequently increasing FM volume fractions. Fluctuations of FM volume fraction could be explained by the hypothesis of austenite reversion, supported by the Kurdjumov – Sachs crystallographic orientation relationship between fine FCC γ-Fe grains and the surrounding BCC α-Fe grain.
2. Microstructure analyses of the 50 wt.% CuCrZr specimen showing different grain size distributions revealed the correlation between cooling rate, IHT, and FM volume fraction. The increase in FM volume fraction is potentially caused by higher cooling rates in specific regions, e.g. layers printed on relatively cooler substrates, as well as less IHT in the top region of the specimens where the cooling rates were relatively constant. This was supported by tomographic scans indicating the influence of gas flow on phase distribution. The correlation between cooling rate and FM volume fraction was explained by the greater degree of Ni entrapment in the Cu-rich liquid upon solidification at higher cooling rates, which is confirmed by thermodynamic simulations.
3. These insights suggest opportunities for further research to control the ferromagnetic phase formation during the manufacturing process and, thus, potentially tailor the mechanical properties of built components.

5. Methods

5.1. Materials characterisation

Gas-atomised, spherical powders of stainless steel 316L (Carpenter Additive, United Kingdom) and CuCrZr (ECKART TLS GmbH, Germany) shown in Supplementary Figure 1 with chemical compositions listed in Supplementary Table 1 were used. Supplementary Table 2 lists the particle size distribution of each powder. The powders were premixed for 4–6 hours using a 3D shaker mixer TURBULA® (Willy A Bachofen AG, Switzerland) to obtain 40, 50, and 60 wt.% mixtures of CuCrZr in 316L powder.

5.2. The n-SLM configurations

Figure 1 shows the high-density infrared laser beam (1) that is collimated, deflected, and focused by the scanning unit (2) onto a working plane with a 20 mm diameter opening (3) for the build plate in the printing chamber (4). In the drive chamber, the build plate, built specimen, and powder are enclosed in an aluminum cylinder holder (5) mounted on several motion

stages, i.e. a rotation stage (6) around the y direction, vertical translation stage (7) along the y direction, goniometer stage (8) around the z direction, and linear translation stage (9) along the x direction, positioned on a wedge with an inclination of 10° in the drive chamber (10). The laser source of the n-SLM is a TruFiber 500 P compact (FD44-W) from TRUMPF Schweiz AG, Switzerland. It has a maximum power of 500 W, a wavelength of 1078–1082 nm, and a beam parameter product of 0.38 ± 0.03 mm.mrad in single mode. The laser beam is collimated, deflected, and focused by a 3-axis or pre-focusing scanning unit AXIALSCAN FIBER-30 (Raylase GmbH, Germany). The focused beam has a Gaussian intensity distribution with a minimum spot diameter of 35 µm measured at $1/e^2$. The laser source and scanning unit are controlled by a SP-ICE-3 control card and the RAYGUIDE software (RAYLASE GmbH, Germany).

The vertical translation stage has a resolution of 0.1 µm and a maximum travel distance of 30 mm, which limits the build height. The rotation stage is required for tomography scans and diffraction measurements along the transverse directions. The goniometer and linear translation stages are specially designed for diffraction measurements along the build direction. The build plate can accommodate structure-borne sensors, e.g. acoustic emission sensor, or be heated to 200°C using a ring heating element and a dedicated ZrO_2 holder. The temperature of the build plate can be monitored by inserting thermocouples underneath. The powder deposition system comprises a hopper-based powder reservoir (11) equipped with stereolithography 3D-printed arms with inlet and outlet gas channels. The channels generate a laminar crossflow of inert gas over the powder bed to extract the by-products, e.g. spatters and plumes, produced during printing. The powder reservoir is driven by a dual-shaft stepper motor (12) via grooved belts and pulleys and is guided by strengthened stainless steel rods.

The inert atmosphere in the chambers is maintained by flushing high-purity Ar gas with a slight overpressure to avoid oxygen contamination. Programmed flow and pressure controllers regulate the flow rate and pressure of the inlet gas. A maximum overpressure of 60 mbar is assured by a safety relief valve fixed on the side of the drive chamber (13). The oxygen level is monitored with an accuracy of +/ – 0.5% by sensors placed in line following the gas outlets of the chambers. The chambers are tightly sealed to avoid leakage of laser light and particles. A series of filters is placed in the inlet and exhaust gas lines to prevent contaminating the inert gas with powder particles. In the chambers, custom-made filter caps (14) made of fine-meshed stainless steel with 2 µm pores are mounted on the gas inlets and outlets. After leaving the chambers and before the oxygen sensors, PTFE membrane filters are placed to sieve particles larger than 0.2 µm escaping the chambers. Subsequent to the oxygen sensor is a water-based filter to entrap the remaining smaller particles.

Two position switches on the cabinet door (15) combined with the E-shutter function of the laser source prevent laser emission when the door is opened. The structure of the device is predominantly made of aluminum alloy EN AW-6082, allowing negligible attenuation of neutrons [60]. Stainless steel 316L is only used for the plate separating the printing chamber and the drive chamber to provide sufficient structural stability and even deposition of powder layers. Consequently, the topmost 2 mm of the specimen is covered by the plate and cannot be probed at that time. Two 7-mm-thick laser safety windows (16) providing high protection levels in the near-infrared range are fixed on the door for observation purposes. Vacuum flanges (17) are welded on the sides of the printing chamber to provide easy access to sensors, e.g. air-borne acoustic emission sensors, optical sensors, and thermal cameras. The system communication, control, and digital interface are established through the Laboratory Virtual Instrument Engineering Workbench (LabVIEW).

5.3. Operando experimental methods

The BOA beamline distinguished by a cold neutron spectrum with a peak wavelength of 2.8 Å and a mean wavelength of 3.8 Å. The beamline is equipped with a permanently installed multi-channel polarising-bender providing polarised neutron beam. Further components required for PNI; an adiabatic fast passage π-spin flipper [61], a magnetic guide field, and a 40×40 mm^2 supermirror neutron spin filter serving as a spin analyser [28] were installed. The high polarisation of the incident beam is preserved by the aligned magnetic guide field, ideally up to the spin analyzer. The specimen to be measured is placed prior to and preferably as close as possible to the analyzer to obtain the optimum resolution on the following imaging detector. Therefore, the n-SLM was mounted between the magnetic guide field and the spin analyzer, as shown in Figure 2.

The neutron imaging detector installed subsequent to the spin analyser consists of a 200 µm thick (LiF/ZnS (Ag)) scintillator screen (RC Tritec AG, Switzerland) fixed on a small scale extension of a light-tight box containing a Zeiss MAKRO-PLANAR 2/100 mm ZF.2 objective lens mounted on an optical Andor iKon-L CCD camera (2048×2048 pixels). An effective pixel size of 50 µm was realised by adjusting the magnification of the lens,

enabling a FoV of 102×102 mm^2. As the probed specimen is enclosed in the n-SLM, the sample-to-detector distance inevitably spans much greater, which deteriorates the spatial resolution. While compensating for the spatial resolution deterioration by reducing the sample-to-detector distance to 8–10 cm, the extension limited the effective FoV to 28×28 mm^2. Another way to compensate for the deterioration is by collimating the beam. However, further beam collimation was not an option since higher flux was intended to achieve adequate statistics in such a short exposure time.

5.4. Post-mortem characterisation

The specimens were removed from the build plate and cut in half parallel to the incident beam direction (TD1) and perpendicular to the build direction (BD). The cut surfaces were ground and mechanically polished with SiC abrasive papers and diamond suspension up to 0.25 µm size for optical microscopy and further polished using MasterMet 2 suspension on a VibroMet® 2 vibratory polisher (Buehler, Germany) for EDX and EBSD analyses. Cross-section images of the specimens were taken using a KEYENCE digital microscope VHX-5000. The as-received powders and the specimens were examined using a field emission gun scanning electron microscope (FEG SEM) Zeiss ULTRA 55 equipped with an EDX analysis system from Oxford Instruments and an EDAX Hikari Camera operated at 25 kV in high current mode with a 120 µm aperture. The density of the produced specimens was determined by cross-sectional optical microscopy and image processing with FIJI software (release 2.14.0) [62]. A small section of $2.2 \times 2.4 \times 7.8$ mm^3 was extracted from the 60 wt.%-CuCrZr specimen for magnetisation tests with an E27 Vibrating Sample Magnetometer (MicroSense, USA).

5.5. Data analysis

In the PBF-LB process, the specimen being printed is enclosed in its corresponding powder. Accordingly, both specimen and powder contribute to the beam depolarisation. Therefore, the final transmitted local beam polarisation can be expressed by.

$$P(x, y) = P_s(x, y)\, P_p(x, y) \tag{3}$$

where the subscripts s and p designate normalised polarisation after transmission of the *specimen* and the *powder*, respectively. P_p is extracted from the surrounding powder through which the beam passes without hitting the specimen. However, the neutron travel paths through the powder l_p contained in a cylindrical holder vary across the FoV depending on the local geometry. To gain insight into the local evolution of η_p throughout printing, several regions of interest (ROIs) of 5×5 pixels were taken across the FoV of each acquired image. The plot in Supplementary Figure 3 indicates the progression of $_p$ in ROIs adjacent to (red) and further away (blue) from the specimen. As no consistent trends between the ROIs were observed, $\overline{\eta_p}$ values of each composition were calculated and used to retrieve the depolarisation coefficient of the specimen η_s as follows

$$\eta_s = \frac{-\log_e P - \overline{\eta_p}\, l_p}{l_s} \tag{4}$$

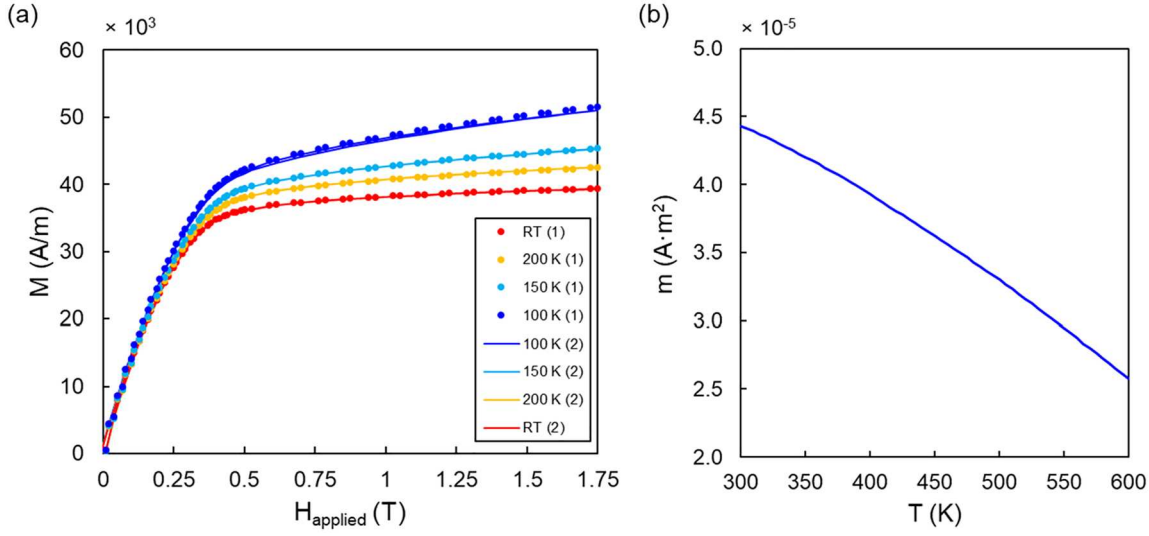

Figure 10. (a) Half of the hysteresis loops and (b) measured magnetic moment of the specimen with 60 wt.% CuCrZr at different temperatures.

where l_s corresponds to the measured thickness of the specimen along the TD1. This method is analogous to that introduced for corresponding attenuation studies in Ref [63].

5.6. Magnetisation measurements

Half of the hysteresis loops of the specimen with 60 wt.% CuCrZr were taken at sequentially decreasing and increasing temperatures, i.e. RT, 200 , 150 , 100 , 100 , 150 , 200 K, and back to RT, as shown in Figure 10(a). As the hysteresis loops acquired at the same temperatures exhibit similar behaviours, no irreversible solid-state phase transformation, for instance, γ-Fe to α′-Fe, occurred. It further supports the assumption that the rapid cooling down phase after the laser was off does not involve displacive phase transformation which may result in an increase in the FM vol.%. The plot in Figure 10(b) is not only useful to estimate $T(x, y, t > t_f)$, but it also verifies that the data obtained from the operando experiments are below the Curie point and, therefore, the change in FM vol.% is solely caused by phase transformations.

Author contributions

Shieren Sumarli: conceptualisation, methodology, resources, investigation, formal analysis, data curation, visualisation, writing – original draft. **Florencia Malamud:** formal analysis, resources, visualisation, validation, writing – review and editing. **Steven Van Petegem:** conceptualisation, resources, formal analysis, funding acquisition, supervision, writing – review and editing. **Steve Gaudez:** investigation, formal analysis, funding acquisition, writing – review and editing. **Antonios Baganis:** methodology, resources, investigation. **Matteo Busi:** formal analysis, resources, investigation, data curation. **Efthymios Polatidis:** conceptualisation, writing – review and editing. **Christian Leinenbach**: funding acquisition, supervision, writing – review and editing. **Roland E. Logé:** funding acquisition, supervision, writing – review and editing. **Markus Strobl:** conceptualisation, methodology, resources, validation, supervision, project administration, funding acquisition, writing – review and editing.

Acknowledgments

S.S. and M.S. thank the CHART-MagDev laboratory at PSI for the support on the specimen preparation equipment. S.S. appreciates Jonathan Charrière from the Laboratory of Quantum Magnetism at EPFL for the support and discussions on experiments with the magnetometer. The generous financial support from PX group to EPFL-LMTM is appreciated.

Disclosure statement

No potential conflict of interest was reported by the author(s).

Funding

This work was supported by the Swiss National Science Foundation (SNSF) under grant agreement No. CRSII5_193799, the Strategic Focus Area Advanced Manufacturing (SFA-AM) programme for the Multi-Mat project, and the European Union's HORIZON EUROPE Marie Sklodowska-Curie Actions 2020 research and innovation programme under grant agreement No. 884104 (PSI-FELLOW-III-3i).

Data availability

The raw data required to reproduce these findings are available to download from https://doi.org/10.5281/zenodo.12565960.

References

[1] Binder M, Anstaett C, Horn M, et al. Potentials and challenges of multi-material processing by laser-based powder bed fusion. 2018 International Solid Freeform Fabrication Symposium; 2018; University of Texas at Austin doi:10.26153/tsw/17025.

[2] Wei C, Zhang Z, Cheng D, et al. An overview of laser-based multiple metallic material additive manufacturing: from macro- to micro-scales. Int J Extreme Manuf. 2021;3(1):012003, doi:10.1088/2631-7990/abce04

[3] Chen J, Yang Y, Song C, et al. Influence mechanism of process parameters on the interfacial characterization of selective laser melting 316L/CuSn10. Mater Sci Eng A. 2020;792:139316, doi:10.1016/j.msea.2020.139316

[4] Chen J, Yang Y, Song C, et al. Interfacial microstructure and mechanical properties of 316L /CuSn10 multi-material bimetallic structure fabricated by selective laser melting. Mater Sci Eng A. 2019;752:75–85. doi:10.1016/j.msea.2019.02.097

[5] Kuai Z, Li Z, Liu B, et al. Microstructure and mechanical properties of CuCrZr/316L hybrid components manufactured using selective laser melting. J Alloys Compd. 2023;955:170103, doi:10.1016/j.jallcom.2023.170103

[6] Mao S, Zhang DZ, Ren Z, et al. Effects of process parameters on interfacial characterization and mechanical properties of 316L/CuCrZr functionally graded material by selective laser melting. J Alloys Compd. 2022;899:163256, doi:10.1016/j.jallcom.2021.163256

[7] Mannucci A, Tomashchuk I, Vignal V, et al. Parametric study of laser welding of copper to austenitic stainless steel. Procedia CIRP. 2018;74:450–455. doi:10.1016/j.procir.2018.08.160

[8] Rinne J, Seffer O, Nothdurft S, et al. Investigations on the weld metal composition and associated weld metal cracking in laser beam welded steel copper dissimilar

joints. J Mater Process Technol. 2021;296:117178, doi:10.1016/j.jmatprotec.2021.117178

[9] Zafari A, Xia K. Nano/ultrafine grained immiscible Fe-Cu alloy with ultrahigh strength produced by selective laser melting. Mater Res Lett. 2021;9(6):247–254. doi:10.1080/21663831.2021.1884620

[10] Zafari A, Xia K. Laser powder bed fusion of ultrahigh strength Fe-Cu alloys using elemental powders. Addit Manuf. 2021;47:102270, doi:10.1016/j.addma.2021.102270

[11] Wen Y, Wu X, Huang A, et al. Laser powder bed fusion of immiscible steel and bronze: A compositional gradient approach for optimum constituent combination. Acta Mater. 2024;264:119572, doi:10.1016/j.actamat.2023.119572

[12] Hu Z, Ma Z, Yu L, et al. Functionally graded materials with grain-size gradients and heterogeneous microstructures achieved by additive manufacturing. Scr Mater. 2023;226:115197, doi:10.1016/j.scriptamat.2022.115197

[13] Martendal CP, Esteves PDB, Deillon L, et al. Effects of beam shaping on copper-steel interfaces in multi-material laser beam powder bed fusion. J Mater Process Technol. 2024;327:118344, doi:10.1016/j.jmatprotec.2024.118344

[14] Xuan Y, Chang J, Ou Y, et al. Heterogeneous structure architected by additive manufacturing: facile route towards strong and ductile steel. Mater Res Lett. 2024;12(3):199–207. doi:10.1080/21663831.2024.2314145

[15] Zhao W, Xiang H, Zhan X, et al. Microstructure evolution in laser powder bed fusion melted 2205 duplex stainless steel using in-situ EBSD during uniaxial tensile testing. J Mater Res Technol. 2024;33:2113–2124. doi:10.1016/j.jmrt.2024.09.218

[16] Cui C, Becker L, Gärtner E, et al. Laser additive manufacturing of duplex stainless steel via powder mixture. J Manuf Mater Process. 2022;6(4). doi:10.3390/jmmp6040072

[17] Platl J, Bodner S, Leitner H, et al. Local microstructural evolution and the role of residual stresses in the phase stability of a laser powder bed fused cold-work tool steel. Mater Charact. 2022;193:112318, doi:10.1016/j.matchar.2022.112318

[18] Esmaeilzadeh R, Hamidi-Nasab M, de Formanoir C, et al. In-situ selective laser heat treatment for microstructural control of additively manufactured Ti-6Al-4V. Addit Manuf. 2023;78:103882, doi:10.1016/j.addma.2023.103882

[19] Zhao C, Fezzaa K, Cunningham RW, et al. Real-time monitoring of laser powder bed fusion process using high-speed X-ray imaging and diffraction. Sci Rep. 2017;7(3602):11. doi:10.1038/s41598-017-03761-2

[20] Goel S, Neikter M, Capek J, et al. Residual stress determination by neutron diffraction in powder bed fusion-built Alloy 718: influence of process parameters and post-treatment. Mater Des. 2020;195:12. doi:10.1016/j.matdes.2020.109045

[21] Polatidis E, Malamud F, Strobl M. Engineering. In: Markus S, Eberhard L, editor. *Neutron imaging*. IOP Publishing; 2024. p. 5-1–5-18. doi:10.1088/978-0-7503-3495-2ch5

[22] Polatidis E, Malamud F, Trtik P. Manufacturing. In: Markus S, Eberhard L, editor. *Neutron imaging*. IOP Publishing; 2024. p. 6-1–6-18. doi:10.1088/978-0-7503-3495-2ch6

[23] Čapek J, Polatidis E, Casati N, et al. Influence of laser powder bed fusion scanning pattern on residual stress and microstructure of alloy 718. Mater Des. 2022;221:110983, doi:10.1016/j.matdes.2022.110983

[24] Polatidis E, Čapek J, Upadhyay MV. Validating texture and lattice strain evolution models via in-situ neutron diffraction and shear tests. Materialia. 2023;28:101752, doi:10.1016/j.mtla.2023.101752

[25] Polatidis E, Morgano M, Malamud F, et al. Neutron diffraction and diffraction contrast imaging for mapping the TRIP effect under load path change. Materials (Basel). 2020;13(6):1450, doi:10.3390/ma13061450

[26] Woracek R, Penumadu D, Kardjilov N, et al. Neutron Bragg edge tomography for phase mapping. Phys Procedia. 2015;69:10. doi:10.1016/j.phpro.2015.07.032

[27] Woracek R, Santisteban J, Fedrigo A, et al. *Diffraction in neutron imaging – a review*. Nucl Instrum Methods Phys Res Sect A. 2018;878:18. doi:10.1016/j.nima.2017.07.040

[28] Busi M, Polatidis E, Sofras C, et al. Polarization contrast neutron imaging of magnetic crystallographic phases. Mater Today Adv. 2022;16:100302, doi:10.1016/j.mtadv.2022.100302

[29] Busi M, Polatidis E, Samothrakitis S, et al. 3D characterization of magnetic phases through neutron polarization contrast tomography. Addit Manuf Lett. 2023;6:100155, doi:10.1016/j.addlet.2023.100155

[30] Kardjilov N, Manke I, Hilger A, et al. Neutron imaging in materials science. Mater Today. 2011;14(6):248–256. doi:10.1016/S1369-7021(11)70139-0

[31] Al-Falahat AAM, Kardjilov N, Woracek R, et al. Temperature dependence in Bragg edge neutron transmission measurements. J Appl Crystallogr. 2022;55(Pt 4):919–928. doi:10.1107/S1600576722006549

[32] Carreon Ruiz ER, Lee J, Strobl M, et al. Revealing the impact of temperature in battery electrolytes via wavelength-resolved neutron imaging. Sci Adv. 2023;9(39):eadi0586. doi:10.1126/sciadv.adi0586

[33] Buchmayr B, Panzl G, Walzl A, et al. Laser powder bed fusion – materials issues and optimized processing parameters for tool steels, AlSiMg- and CuCrZr-alloys. Adv Eng Mater. 2017;19(4):1600667. doi:10.1002/adem.201600667

[34] Wallis C, Buchmayr B. Effect of heat treatments on microstructure and properties of CuCrZr produced by laser-powder bed fusion. Mater Sci Eng A. 2019;744:215–223. doi:10.1016/j.msea.2018.12.017

[35] Zhang K, Gaganidze E, Gorley M. Development of the material property handbook and database of CuCrZr. Fusion Eng Des. 2019;144:148–153. doi:10.1016/j.fusengdes.2019.04.094

[36] Morgano M, Peetermans S, Lehmann EH, et al. Neutron imaging options at the BOA beamline at Paul Scherrer Institut. Nucl Instrum Methods Phys Res Sect A. 2014;754:46–56. doi:10.1016/j.nima.2014.03.055

[37] Brandau B, Da Silva A, Wilsnack C, et al. Absorbance study of powder conditions for laser additive manufacturing. Mater Des. 2022;216:110591, doi:10.1016/j.matdes.2022.110591

[38] Burgy M, Hughes DJ, Wallace JR, et al. Double transmission and depolarization of neutrons. Phys Rev. 1950;80(6):953–960. doi:10.1103/PhysRev.80.953

[39] Halpern O, Holstein T. On the passage of neutrons through ferromagnets. Phys Rev. 1941;59(12):960–981. doi:10.1103/PhysRev.59.960
[40] Buttle D, Scruby C. Residual stresses: measurement using magnetoelastic effects. In: KHJ Buschow, editor. *Encyclopedia of materials: science and technology*. Oxford: Elsevier; 2001. p. 8173–8180. doi:10.1016/B0-08-043152-6/01465-0
[41] Lindquist AK, Feinberg JM, Harrison RJ, et al. Domain wall pinning and dislocations: investigating magnetite deformed under conditions analogous to nature using transmission electron microscopy. J Geophys Res: Solid Earth. 2015;120(3):1415–1430. doi:10.1002/2014JB011335
[42] Liu L, Ding Q, Zhong Y, et al. Dislocation network in additive manufactured steel breaks strength–ductility trade-off. Mater Today. 2018;21(4):354–361. doi:10.1016/j.mattod.2017.11.004
[43] Wang G, Ouyang H, Fan C, et al. The origin of high-density dislocations in additively manufactured metals. Mater Res Lett. 2020;8(8):283–290. doi:10.1080/21663831.2020.1751739
[44] Bertsch KM, De Bellefon GM, Kuehl B, et al. Origin of dislocation structures in an additively manufactured austenitic stainless steel 316L. Acta Mater. 2020;199:19–33. doi:10.1016/j.actamat.2020.07.063
[45] Cai XX, Kittelmann T. NCrystal: A library for thermal neutron transport. Comput Phys Commun. 2020;246:106851, doi:10.1016/j.cpc.2019.07.015
[46] Damon J, Koch R, Kaiser D, et al. Process development and impact of intrinsic heat treatment on the mechanical performance of selective laser melted AISI 4140. Addit Manuf. 2019;28:275–284. doi:10.1016/j.addma.2019.05.012
[47] Kang N, Coniglio N, Cao Y, et al. Intrinsic heat treatment induced graded surficial microstructure and tribological properties of selective laser melted titanium. J Tribol. 2021;143(5). doi:10.1115/1.4049701
[48] Kurdjumow G, Sachs G. Über den Mechanismus der Stahlhärtung. Zeitschrift für Physik. 1930;64(5):325–343. doi:10.1007/BF01397346
[49] Niessen F, Nyyssönen T, Gazder AA, et al. Parent grain reconstruction from partially or fully transformed microstructures in MTEX. J Appl Crystallogr. 2022;55(1):180–194. doi:10.1107/S1600576721011560
[50] Naraghi R. (2009). *Martensitic transformation in austenitic stainless steels*.
[51] Ohtsuka H, Ghosh G, Nagai K. Effects of Cu on diffusional transformation behavior and microstructure in Fe-Mn-Si-C steels. ISIJ Int. 1997;37(3):296–301. doi::10.2355/isijinternational.37.296
[52] Mooraj S, Feng S, Luebbe M, et al. Martensitic transformation induced strength-ductility synergy in additively manufactured maraging 250 steel by thermal history engineering. J Mater Sci Technol. 2024;211:212–225. doi:10.1016/j.jmst.2024.05.062
[53] Krakhmalev P, Yadroitsava I, Fredriksson G, et al. In situ heat treatment in selective laser melted martensitic AISI 420 stainless steels. Mater Des. 2015;87:380–385. doi:10.1016/j.matdes.2015.08.045
[54] Takeuchi A, Inoue A. Mixing enthalpy of liquid phase calculated by Miedema's scheme and approximated with sub-regular solution model for assessing forming ability of amorphous and glassy alloys. Intermetallics. 2010;18(9):1779–1789. doi:10.1016/j.intermet.2010.06.003
[55] Arabi-Hashemi A, Maeder X, Figi R, et al. 3D magnetic patterning in additive manufacturing via site-specific in-situ alloy modification. Appl Mater Today. 2020;18:100512, doi:10.1016/j.apmt.2019.100512
[56] Ferretto I, Borzi A, Kim D, et al. Control of microstructure and shape memory properties of a Fe-Mn-Si-based shape memory alloy during laser powder bed fusion. Addit Manuf Lett. 2022;3:100091, doi:10.1016/j.addlet.2022.100091
[57] Perez M, Perrard F, Massardier V, et al. Low-temperature solubility of copper in iron: experimental study using thermoelectric power, small angle X-ray scattering and tomographic atom probe. Philos Mag. 2005;85(20):2197–2210. doi:10.1080/14786430500079645
[58] Salje G, Feller-Kniepmeier M. The diffusion and solubility of iron in copper. J Appl Phys. 1978;49(1):229–232. doi:10.1063/1.324336
[59] Andersson JO, Helander T, Höglund L, et al. Thermo-Calc & DICTRA, computational tools for materials science. Calphad. 2002;26(2):273–312. doi:10.1016/S0364-5916(02)00037-8
[60] Vontobel P, Lehmann E, Frei G. Performance characteristics of the tomography setup at the PSI NEUTRA thermal neutron radiography facility. Proc Comput Tomogr Image Proc Ind Radiol. 2003;35:23–25.
[61] Babcock E, Petoukhov A, Chastagnier J, et al. AFP flipper devices: polarized 3He spin flipper and shorter wavelength neutron flipper. Phys B. 2007;397(1):172–175. doi:10.1016/j.physb.2007.02.093
[62] Schindelin J, Arganda-Carreras I, Frise E, et al. Fiji: an open-source platform for biological-image analysis. Nat Methods. 2012;9(7):676–682. doi:10.1038/nmeth.2019
[63] Sumarli S, Polatidis E, Malamud F, et al. Neutron Bragg edge imaging for strain characterization in powder bed additive manufacturing environments. J Mater Res Technol. 2022;21:30–39. doi:10.1016/j.jmrt.2022.11.047